Assessment of the application of an off-shelf fuel cell turbocompressor for low temperature refrigeration for cryogenic carbon capture

Ivo M. Cabral[a], João S. Pereira[a], José B. Ribeiro[a]

[a] Univ. Coimbra, ADAI, Department of Mechanical Engineering, Rua Luís Reis Santos, Polo II, 3030-788 Coimbra, ivo.cabral@adai.pt,CA

Abstract:

Cryogenic Carbon Capture (CCC) is a promising technology for industrial decarbonization, although its widespread adoption is often hindered by high energy demands and component costs. Additionally, the typical vapor-compression refrigeration cycles for very low temperatures, used in this application, have faced increasing regulatory pressure due to the phase-down of high global warming potential (GWP) refrigerants. This has brought to light the importance of air cycles and direct refrigeration through gas expansion. However, this approach typically suffers from very high component costs.

This paper's objective is to perform a preliminary assessment of a off-the-shelf fuel cell turbocompressors as active cooling components within a CCC framework. For that purpose, a semi-empirical model is developed and described based on the turbocompressor characteristic curves and the governing thermodynamic principles. Afterwards, experimental results are compared with the model's prediction allowing for its validation and the assessment of the performance indicators such as the cooling capacity.

Early results show the potential for the turbocompressor to operate at very low temperatures with remarkable refrigeration capacity. Additionally, when utilized as the last step to go from low to ultra-low temperatures it provided similar values of coefficient of performance compared with stand-alone vapor compression refrigeration systems while being a simpler and almost maintenance free system. The findings provide critical insights into the viability of utilizing off-the-shelf hardware for very low temperature refrigeration applications, highlighting the trade-offs between cost-efficiency and thermodynamic performance in carbon mitigation systems.

Keywords:

Air refrigeration cycle; Cryogenic Carbon Capture; Expansion cooling; Fuel-cell turbocompressor; Ultra-low temperature Refrigeration.

1. Introduction

Carbon capture technologies are critical for mitigating rising atmospheric CO_2 concentrations [1]. Within this field, Cryogenic Carbon Capture (CCC) has emerged as a promising solution for deep decarbonization of hard-to-abate sectors and low-concentration point sources. Unlike mature alternatives, CCC leverages the thermodynamic properties of CO_2 at cryogenic temperatures to achieve separation through phase change [2]. While separation can occur via condensation/distillation or reverse sublimation, the latter is increasingly preferred for low-concentration sources. By allowing CO_2 to transition directly to a solid phase, reverse sublimation avoids the energy-intensive pressurisation required to operate above the triple point (217 K, 518 kPa), achieving purities exceeding 99.9% while simultaneously removing pollutants like mercury and sulphur oxides [2,3]. However, widespread CCC adoption is hindered by the high energy intensity of reaching 100 K, significant capital expenditure (CAPEX), and a shifting regulatory landscape [2,4].

Historically, CCC relied on vapor-compression refrigeration cycles (VCRC) using synthetic refrigerants [3]. These fluids are now under intense scrutiny with the Kigali Amendment mandating an 80% global phase-down of hydrofluorocarbons (HFCs) by 2045 [5], leading to the 2025 discontinuation of high-GWP refrigerants like R22 and R134A [4]. While ultra-low temperature (ULT) applications (<220 K) initially avoided strict regulation, the EU F-gas Regulation (2024/573) aims to prohibit all fluorinated refrigerants with a GWP >150 by 2030, targeting a total HFC phase-out by 2050 [6–8]. Consequently, research has pivoted toward natural alternatives. According to the European Commission, air (R-729) is one of the safest viable ULT options (ASHRAE A1) [8]. Additionally, while VCRC systems typically offer higher Coefficients of Performance (COP) at moderate temperatures, the Air Refrigeration Cycle (ARC) still becomes competitive at ultra-low depths [6]. Furthermore,

ARC systems typically utilize a reverse Brayton cycle, a proven method in aviation air conditioning and air liquefaction units, that eliminates synthetic refrigerants [9].

The primary barrier to ARC remains the high cost of precisely engineered turboexpanders, which often represent the system's largest capital investment [10]. To mitigate CAPEX, recent studies have explored repurposing mass-produced components. Efforts include adapting automotive turbochargers for data center cooling [11] or modifying their housings and lubrication systems to achieve lower temperatures with high isentropic efficiencies, reaching 85% [11,12]. Alternatively, aviation Air Cycle Machines (ACM) offer high performance and oil-free aerodynamic bearings but lack the cost advantages of true mass production [9,12]. Therefore, Fuel-cell turbocompressors represent a strategic "middle ground." Designed also for the transport sector, these mass-produced units feature integrated high-speed motors and aerodynamic bearings, yet their potential for ARC applications remains largely unexplored [13].

This work presents a preliminary assessment of an off-the-shelf fuel-cell turbocompressor for expansion cooling of ambient air to cryogenic temperatures. We develop a semi-empirical model based on component operating curves and perform a parametric analysis to estimate performance. Finally, we detail an experimental apparatus and analyze a battery of tests to validate the model and assess the turbocompressor's refrigeration capacity.

2. Fuel cell turbocompressor semi-empirical model

Modelling a turbocompressor can be performed by two main paths: a) a physical model and b) a semi-empirical model. The first option requires the knowledge of the geometry of both the compressor and turbine wheels in detail, which is commonly information that is not made available by manufacturers. Therefore, the second option is commonly the chosen method, where experimental data regarding both the compressor and turbine is gathered and provided as a reference. For that reason, the first step is to select a turbocompressor. For this work, the selected turbocompressor is the Fischer ® EMTCT-120k-Air-Gen 4.2, and its main characteristics are aggregated in Table 1.

Table 1. Main operational parameters of the Fischer ® EMTCT-120k-Air-Gen 4.2. Adapted from *[14]*.

Bearing	Max. coolant temperature, K	Max. pressure ratio	Max. air flow, kg/s	Max. efficiency	Inlet temperature range, K
Aerodynamic gas bearing	338 @ 6 l/min	3.0	0.145	Compressor: > 70% Turbine: > 80%	Compressor: [233 – 333] Turbine: [233 – 393]

This turbocompressor was mainly selected due to its very wide range of operation and the high efficiencies. Alongside the component, the manufacturer also provided the respective compressor and turbine maps of operation. These maps provide the relation between pressure ratio (PR), isentropic efficiency (η_{isen}), motor speed (ω), DC power input ($\dot{P}_{DC}$), and mass flow ($\dot{m}$) in a normalized manner to allow for result extrapolation. Therefore, to produce the semi-empirical model, there is a need to establish the proper thermodynamic principles and assumptions.

2.1. Physical principles

Both the compressor and turbine are very complex components to model in detail due to interacting fluid and thermodynamic phenomena. Despite this, from a thermodynamic point of view, the modelling of these components can be simplified. Considering both components adiabatic, the thermodynamic transformation that occurs, if ideal, would be isentropic. However, it is known that these components produce irreversibility, which can be accounted for by determining the respective η_{isen}. For that reason, both components can be thermodynamically modelled by resorting to Equations (1) and (2) for the compressor and turbine, respectively.

$$h_{out,real} = (h_{out,isen} - h_{in})/\,\eta_{isen} + h_{in}, \quad (1)$$

$$h_{out,real} = \; h_{in} - \eta_{isen} \times (h_{in} - h_{out,isen}). \quad (2)$$

In both equations, h indicates the enthalpy of the fluid stream, the subscripts out and in are used to define whether we are considering the enthalpy at the inlet or outlet of the component. The subscript $isen$ is used to define the enthalpy that should be determined considering the isentropic condition. Having established the PR, the η_{isen}, the inlet temperature and pressure, is possible to determine the outlet thermodynamic conditions.

After, the work performed by both components, can be estimated resorting to an energy balance considering the inlet and outlet conditions, as is represented in Equations (3) and (4) for the compressor and turbine, respectively.

$$\dot{W}_c = \dot{m} \times (h_{out,real} - h_{in}), \quad (3)$$

$$\dot{W}_t = \dot{m} \times (h_{in} - h_{out,real}). \quad (4)$$

In Eqs. (3) and (4) the variable $\dot{W}$ represents the work performed by the component to analyse and $\dot{m}$ the respective mass flow. The subscripts c and t, represent that the variable refers to the compressor and turbine, respectively.

For the composition of the fluid, since in this work the testing will occur with ambient air, the main components of dry ambient air were considered for simplicity of analysis. This resulted in an approximate mole fraction of 0.8 for nitrogen (N_2) and 0.2 for molecular oxygen (O_2). Additionally, to determine the thermodynamic properties, it was considered to be a real fluid, meaning that two properties are needed to determine its thermodynamic state.

2.2. Methodology

For the implementation model and data treatment, the software Matlab® was used. Additionally, it is important to state that the REFPROP database [15] was used to determine the fluid thermodynamic properties throughout the semi-empirical model.

The first step was to compile the empirical data provided by the turbocompressor manufacturer and use the fitting functions from the Matlab® toolboxes to find suitable equations to describe the experimental data, using the minimization of the R-squared (R^2) as the main criteria. The results can be seen in Figure 1 and Figure 2 for the compressor and turbine, respectively.

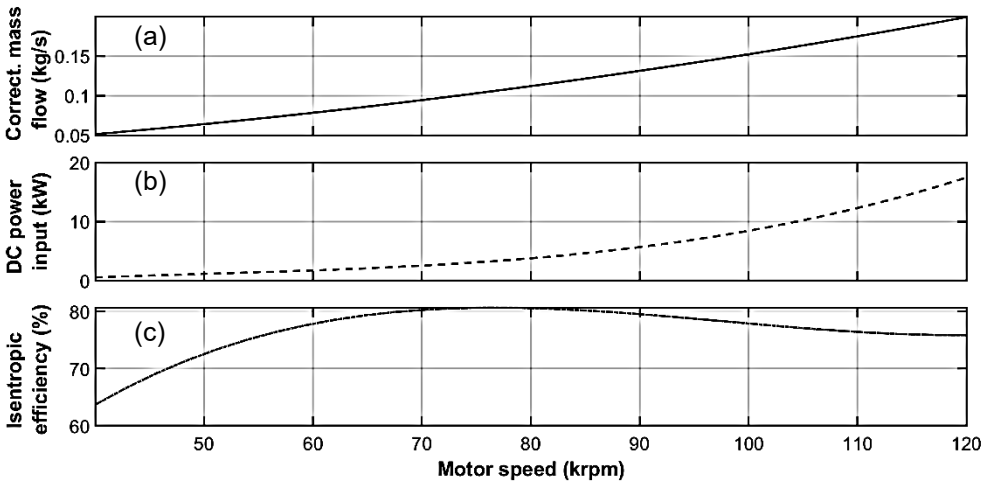

Figure. 1. *Compressor characteristic curves: a) Motor velocity and corrected mass flow, b) motor velocity and DC power input, and c) Motor velocity and isentropic efficiency.*

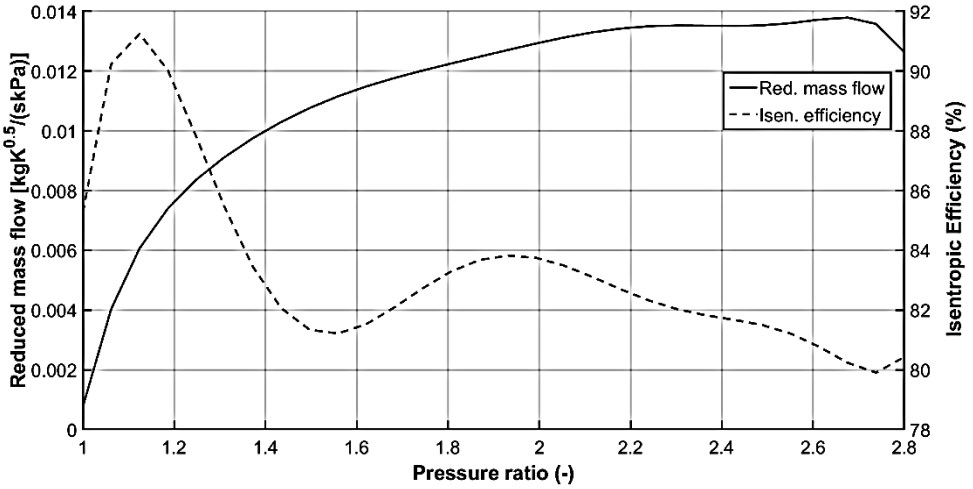

Figure. 2. *Turbine characteristic curves: a) Pressure ratio and reduced mass flow, and b) pressure ratio and isentropic efficiency.*

The constructed model followed a simple configuration with the only components in the system being the compressor and the turbine. At first, the inlet conditions are defined including the motor speed (ω), molar fractions, temperature ($T_{in,c}$) and pressure ($P_{in,c}$) at the inlet of the compressor and temperature at the inlet of the turbine. Since the mass flow is directly dependent on the rotational speed, resorting to the compressor characteristic curve a). The corrected mass flow ($\dot{m}_{corrected}$) is a parameter used as input on the compressor map that can be determined by resorting to Equation (5).

$$\dot{m}_{corrected} = \dot{m} \times [\sqrt{(T_{in,c}/298)}/(P_{in,c}/100)]. \quad (5)$$

In Eq. 3, the presented constants represent the input conditions used by the manufacturer during testing, more specifically, 298 K and 100 kPa. After, the isentropic efficiency can be determined simply by resorting to the compressor characteristic curve c). One of the most important parameters to characterize the impact of the compressor on the fluid is the pressure ratio (PR_c). This parameter will be dependent on the imposed pressure ratio on the turbine (PR_t), which, in turn, is also dependent on the turbine inlet conditions. Therefore, first an estimation of the PR_c is imposed and after this value will be iteratively updated to achieve a PR match. After resorting to Eq. (1), the compressor outlet conditions are determined. After this, the turbine inlet pressure $P_{in,t}$ will be equal to the compressor outlet and the turbine inlet temperature ($T_{in,t}$) will be defined accordingly. Subsequently, the turbine is modelled similarly to the compressor. First, there is the need to determine the PRt resorting to the reduced mass flow ($\dot{m}_{reduced}$) and the turbine characteristic curve a). The reduced mass flow is obtained through Equation (6).

$$\dot{m}_{reduced} = \dot{m} \times (\sqrt{T_{in,t}}/P_{in,t}). \quad (6)$$

With the value of PRt is also possible to determine the turbine isentropic efficiency ($\eta_{isen,t}$) resorting to the turbine characteristic curve b). After the similarity of both the PRc and PRt is evaluated. If different, the assumed value for the pressure ratio of the compressor is altered, and the calculation restarts. This is done iteratively, resorting to the fixed-point iteration method where the pressure ratio from the compressor is altered according to Equation (7).

$$PR_c = 0.8 \times PR_c + 0.2 \times PR_t. \quad (7)$$

In Eq. (7), the weights were selected based on a balance between rapid convergence and variable volatility since PRt is determined using a curve that was estimated through experimental data, which can return highly variable results when reaching for the solution.

When a match between PRc and PRt is achieved, the thermodynamic modelling of the turbine can proceed. The outlet turbine enthalpy can be determined resorting to Eq. (2) and the value of $\eta_{isen,t}$. Consequently, the outlet temperature ($T_{out,t}$) can be determined. After this, the performance indicators can be determined, such as the cooling capacity, which will correspond to the work recovered in the turbine, since at this point, it is considered a simple open cycle operation. Another relevant indicator is the coefficient of performance (COP) that, in this case, since the total DC power input ($\dot{P}_{DC}$) can also be determined empirically with the compressor characteristic curve b), is determined resorting to Equation (8).

$$COP = \dot{W}_t/\dot{P}_{DC}. \quad (8)$$

The aforementioned methodology is demonstrated in the flowchart presented in Figure 3.

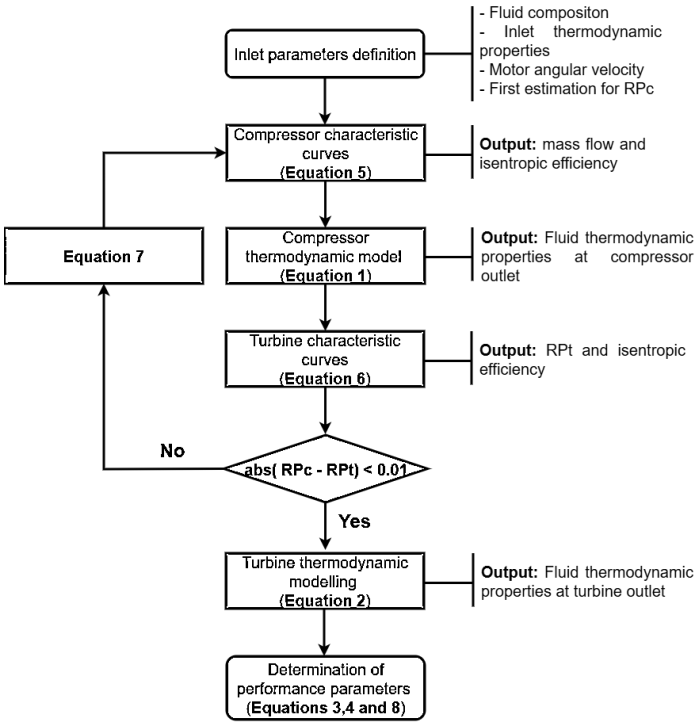

Figure. 3. *Model implementation flowchart.*

2.3. Model exploration

With the model implemented in Matlab®, a parametric analysis must be carried out to analyze the sensitivity to each input variable. Therefore, first, the baseline parameters are defined. After the reference values are established, the variation range is determined, taking into account the component operational limits and a realistic operation of the system. These parameters are compiled in Table 2.

Table 2. *Parametric analysis: Baseline values and variation ranges.*

Variables	Baseline values	Variation range
Molar fractions, %vol	0.8 N_2 and 0.2 O_2	[-]
ω, krpm	80	[40 – 120]
Pin,c, kPa	100	[60 – 120]
Tin,c, K	298	[273 – 333]
Tin,t, K	298	[233 – 333]

It is to highlight that inlet temperatures were defined based on the specific application.

First, the sensitivity analysis is carried out by addressing each variable individually, and assessing their impact on COP, real mass flow and $T_{out,t}$. In order to easily compare the impact of each variable, a normalization was made to consider the percentage of variation in relation to the minimum value of the testing range individually. Therefore, on the x-axis, the values will be measured in percentage of variation. The results can be seen in Figure 4.

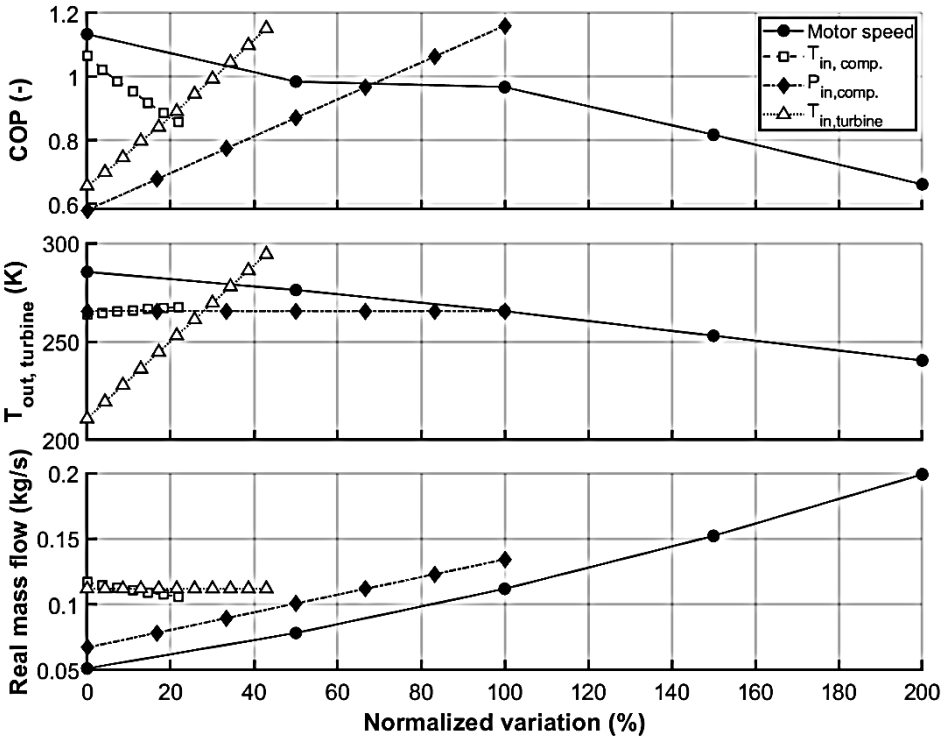

Figure. 4. *Sensitivity analysis results compiling the impact on COP, turbine outlet temperature, net DC power input, and real mass flow.*

By analyzing Figure 4, it is possible to verify that the variables that mostly affect the performance indicators are the ω, $P_{in,c}$ and $T_{in,c}$. The motor speed (ω) is the main controllable parameter, and as it is possible to verify, it is directly connected with the real mass flow passing through the turbocompressor. This, in turn, explains the impact on the other two indicators since higher real mass flows will result in higher PR values which consequently will decrease $T_{out,t}$, reaching a minimum value of 240 K. Despite this, the COP decreases from almost 1.2 to 0.65. This is due to the accelerating growth in $\dot{P}_{DC}$ with the increasing ω that can be seen in Figure 1.

After the $T_{in,t}$ is one of the most influential variables since it directly impacts the $T_{out,t}$ and COP. The data shows that with an inlet temperature of 233 K is possible to reach temperatures as low as 210 K, representing a plus 20-degree temperature difference, while for 333 K inlet temperature, for the tested conditions, the temperature to reach at the outlet will be around 294 K. The difference obtained in temperature variation is a result of the varying reduced mass flow in the turbine, leading to varying PR values. This, in turn, justifies the variation observed in COP values.

Adding to the previous variables, $P_{in,c}$ is also a relevant variable to consider. Its impact on the real mass flow can be indirectly quantified by looking at Eq. (5), which makes it possible to infer that higher pressures will result in higher real mass flow. The most interesting fact is that for higher pressures the COP value increases while the $T_{out,t}$ does not significantly vary. This can be inferred by looking at Eq. (6) where the $\dot{m}_{reduced}$ depends on both the real mass flow and $P_{in,t}$. If there is an increase on $P_{in,c}$, this would result in higher $P_{in,t}$ which counters the higher real mass flow and, consequently, maintains the PR. However, the COP value does increase due to the fact that higher real mass flow values will lead to an increase in the $\dot{W}_t$.

Finally, it can be concluded by analysing Figure 4 that the $T_{in,c}$ is the least meaningful variable since its impact on the real mass flow and $T_{out,t}$ is not significant. Additionally, its impact on the COP value is related to an increase in the $T_{in,c}$, which leads to a decrease in real mass flow values. Nevertheless, the impact of this variable should be analysed carefully since in this case we impose a temperature at the inlet of the turbine regardless of the compressor outlet temperature ($T_{out,c}$). In a real system with a heat exchanger, this might not be the case, and the turbine inlet temperature can start to increase, which would result in higher turbine outlet temperatures.

As an overview of the model results, it is possible to verify that for higher refrigeration temperatures, the obtained COP values are still not competitive to typical VCRC, which is in accordance with the conclusions taken by Saeed, M. Z. et al. [6]. Nevertheless, it is important to highlight that this preliminary analysis considered a simple air open cycle with no optimization. Nevertheless, it already obtained COP values, for reaching temperatures around 210 K, when considering an inlet turbine temperature of around 233 K, of nearly 0.65. This system, coupled with typical COP values for VCRC for the refrigeration between 313 K and 233 K

which, according to [6] could reach values of 1.6 and for which is easier to find more environmentally friendly options, could result in a compound COP of 1.04 which, if validated, represents values of overall performance similar or even higher than a stand-alone VCRC.

With the parametric analysis completed, it is time to proceed with the development of a test rig that will allow for the result validation through real-world testing.

3. Experimental evaluation

This section aims to approach all the developed experimental results, starting from describing the used experimental test rig and testing procedure, and ending with a thorough assessment of the obtained results.

3.1. Experimental apparatus

A test rig was developed to allow for the turbocompressor to be operated in an open cycle configuration with ambient air. An open-air cycle is composed mainly by 3 components: i) the compressor, which will pressurize the gaseous stream in a partially isentropic transformation, ii) a heat exchanger where the heat generated by the compression stage is dissipated, and iii) the turbine that will be responsible for the expansion cooling of the working fluid. Adding to this, the considered turbocompressor is composed of an electric motor and a control unit (Inverter), which require separate heat dissipation. Therefore, the system is divided into three main circuits: a) Air circuit (AC), b) Water/Glycol loop (WGL), c) Heat dissipation circuit (HDC). These circuits can be observed in more detail on the schematic diagram and photographs shown in Figures 5 and 6, respectively.

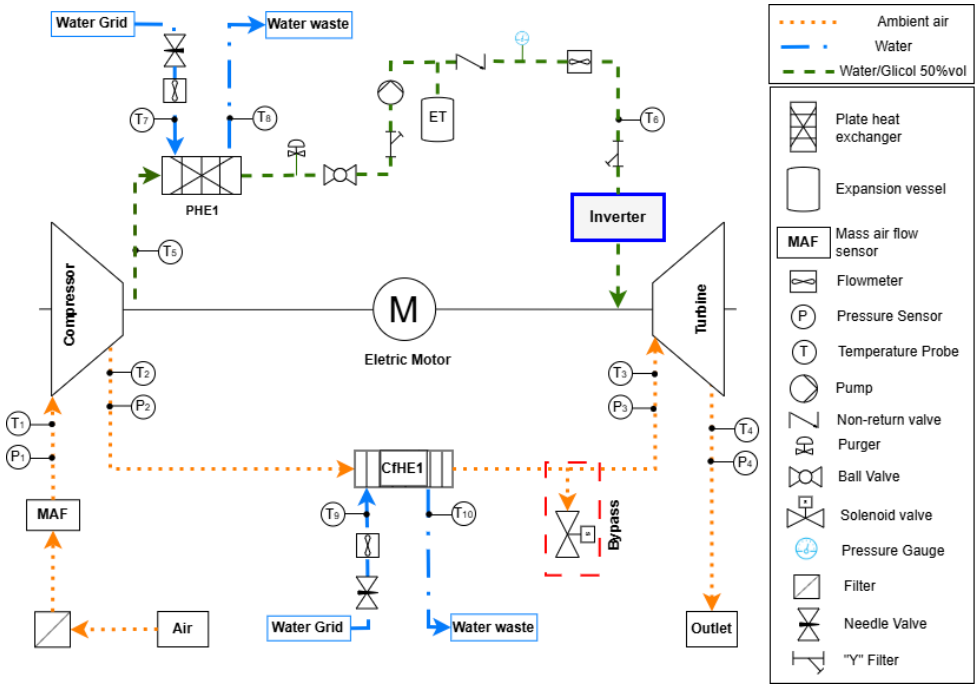

Figure. 5. *Schematic diagram of the experimental test rig.*

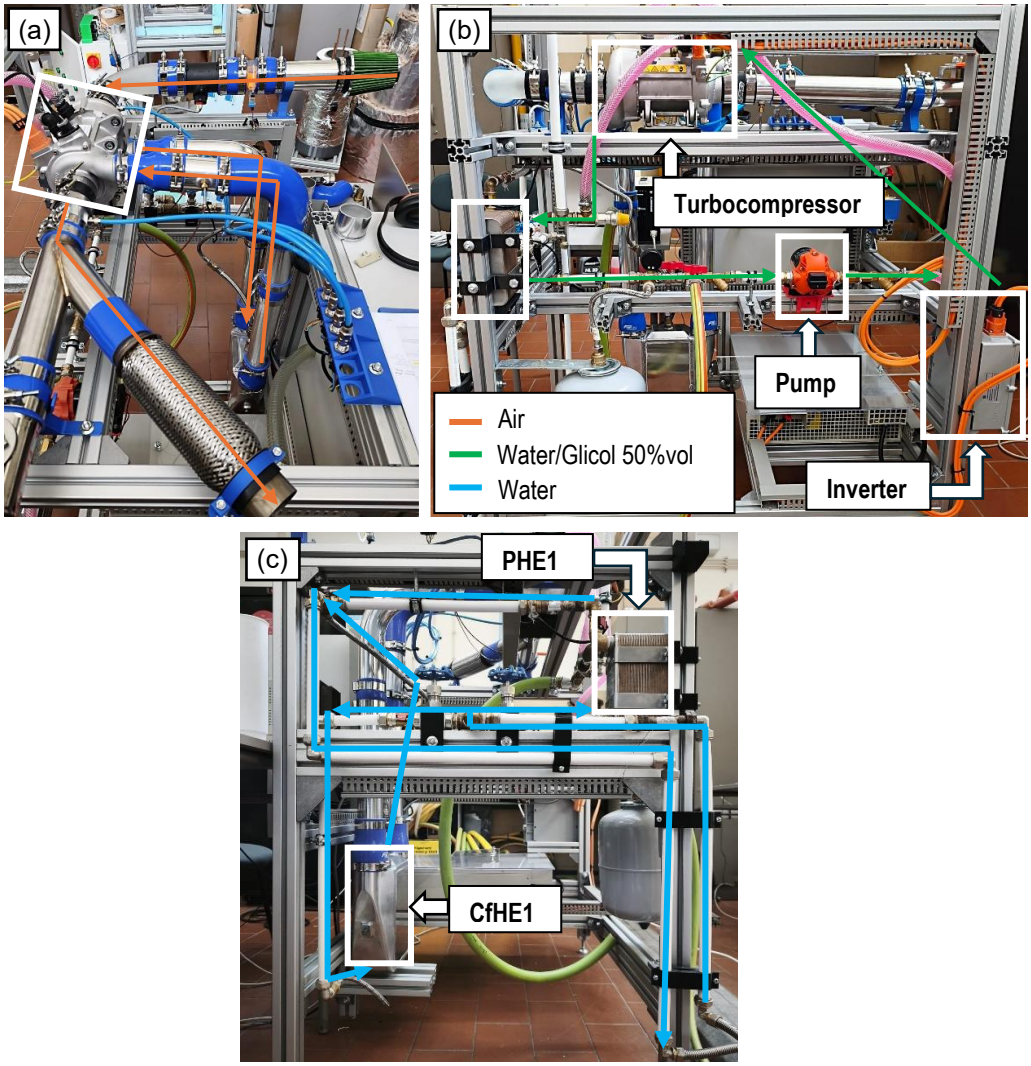

Figure. 6. *Photographs of the experimental test rig: a) upper view, b) rear view, and c) right side view.*

The main circuit is the AC, where the main components are the turbocompressor and the heat exchanger, CfHE1. It is to highlight that for the heat exchanger, an automotive water-gas intercooler was selected based on the range of mass flow of operation. It consists of a highly compact crossflow heat exchanger. From Figure 5, it is possible to verify that this AC also included a bypass valve between the compressor and turbine, which is a recommendation by the manufacturer to promote a safe operation of the system. Regarding the WGL, this circuit is necessary to avoid overheating of the Inverter and the motor of the turbocompressor. The imposed requirements from the manufacturer were a minimum volume flow of 6 (L/min) and a mixture of water and glycol at 50 (%vol) to mitigate corrosion. Therefore, a closed loop had to be developed specifically for this end. The main components of this system, apart from the safety components and instruments, are the turbocompressor motor, the Inverter, the plate heat exchanger (PHE1) to promote heat dissipation for the environment, and the fixed speed diaphragm pump. Finally, the HDC makes use of the water grid to provide the heat dissipation needed for both the AC and WGL. The main components are, besides instrumentation, needle valves to control the mass flow of water used in both cycles.

At this point, it is possible to infer through the description of the test rig that two variables will be controlled: a) ω and b) $T_{in,t}$. This already allows for a preliminary validation of the semi-empirical model and the assessment of the application of this component for low and ultra-low temperature refrigeration.

For the compressor powering, a high-voltage DC power supply was selected according to the manufacturer's specifications. However, it is important to state that due to power limitations at the laboratory, the maximum power consumption allowed is limited to 9 kW, resulting in a limitation of the motor velocity to 90 (krpm).

3.2. Experimental testing

The testing procedure consisted in varying the motor speed between 40 krpm and 90 krpm in steps of 10 krpm and, for each speed value, the water mass flow through the heat exchanger CfHE1 was altered starting from zero and was then increased randomly to achieve different temperatures at the turbine inlet. The considered values were selected when $T_{in,turbine}$ variation was lower than 1 degree for 1 minute. Additionally, the ambient temperature was fixed at 292.5 K, and the inlet pressure had almost no variation throughout testing having values between 99 kPa and 97 kPa for lower and higher motor speed, respectively.

With the aim to consider all the gathered experimental results the most relevant variables were compiled into three groups: a) evaluation of the max pressure ratio and isentropic efficiency of both the compressor and turbine that is present in Figure 7, b) relating both the power consumption and the outlet turbine temperature with the motor speed and turbine inlet temperature present in Figure 8, and c) relating the cooling power and COP with the motor speed and turbine inlet temperature as can be seen in Figure 9. It is to highlight that $T_{in,t}$ increases from the left to the right side. The previous figures are presented next.

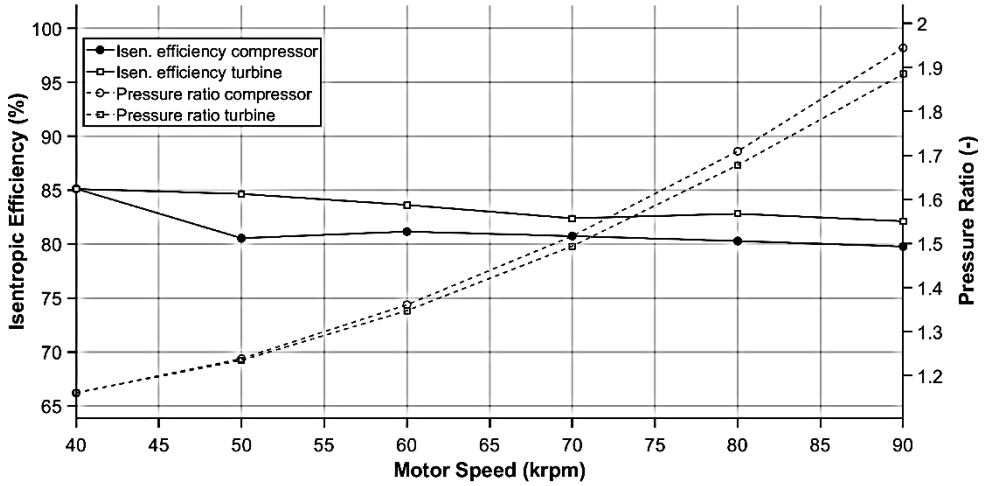

Figure. 7. *Experimental data: Isentropic efficiency and pressure ratio with the motor speed variation.*

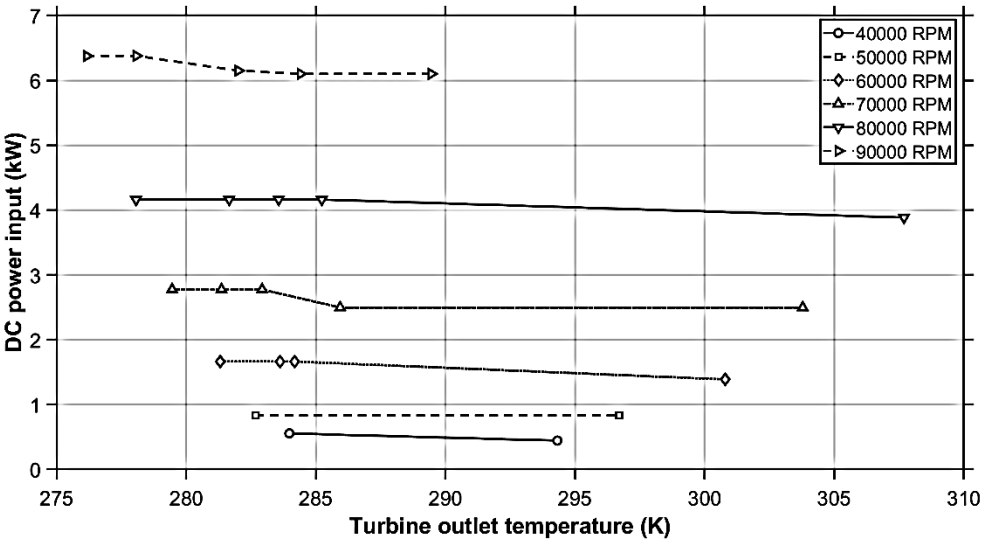

Figure. 8. *Experimental data: DC power input and turbine outlet temperature regarding motor speed.*

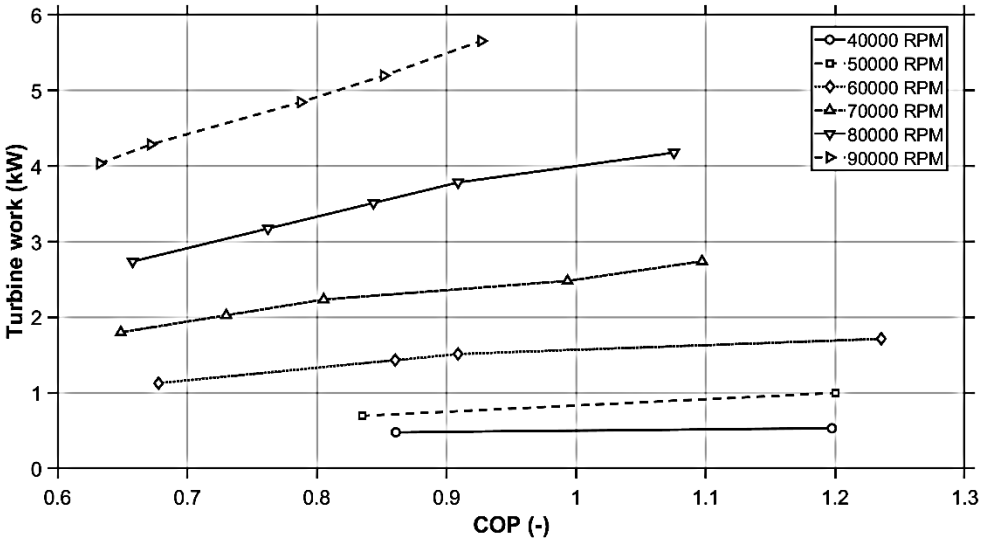

Figure. 9. *Experimental data: Turbine work and COP regarding motor speed.*

First, it is possible to determine from Figures 7 to 9 that the experimental apparatus allowed for a wide range of operation, with several points being gathered regarding both motor speed and turbine inlet temperature variation. Regarding Figure 7, it is possible to draw two main conclusions. The first one is that, similarly to the modelled results, the turbine consistently provided higher isentropic efficiencies than the compressor. While it is also to highlight that the compressor obtained higher results than estimated. On the other hand, the pressure ratio from the compressor and turbine was considered to be equal in the model. However, the experimental results show that this disparity exists and increases with the motor speed. This is a result of the pressure loss between the compressor outlet and the turbine inlet, which impacted the PR_t in about 3%. In Figure 8 and 9 is possible to conclude higher velocities result in higher $\dot{P}_{DC}$ and $\dot{W}_t$ reaching values of between 6 and 6.5 kW for the first and between 4 and 5.8 kW for the second. Adding to this, the higher the ω, the lower the COP values reaching a minimum value for 90 krpm and 308 K of 0.63. This happens due to the fact that the $\dot{P}_{DC}$ increase is not linear with the ω as is possible to visualize in Figure 10. Is also possible to verify from Figure 8 that lower $T_{in,t}$ leads to a slight $\dot{P}_{DC}$ increase and to lower $T_{out,t}$ reaching values as low as 276 K.

In order to assess the model's compliance with the experimental data despite the recognized simplifications, a parity analysis has been made. This analysis is a mostly graphical method to evaluate the predictive accuracy of the mathematical models against experimental observations. The first step is using similar input parameters for the model calculation in order to easily compare the results. After this, the graphical assessment is constructed, starting by defining the x-axis as the experimental results and the y-axis as the model results. Afterwards, the identity line should be defined, representing the condition of perfect prediction. This is done by defining a line that passes through the origin (0,0) and has a constant slope of 1. This analysis insights are threefold: i) it gives insights into accuracy which is directly related to the proximity of the data points to the identity line, ii) allows for systematic errors to be identified by evaluating if the model consistently overestimates (points above the identity line) or underestimates the results (points below the identity line), and iii) provides insights into the model reliability throughout the tested data by including error bands.

For this assessment, the variables to evaluate were COP, $T_{out,t}$, real mass flow, and $\dot{P}_{DC}$. Additionally, to promote an easier comprehension of the overall model error, a 10% error band was introduced into the analysis. The results are presented in Figure 10.

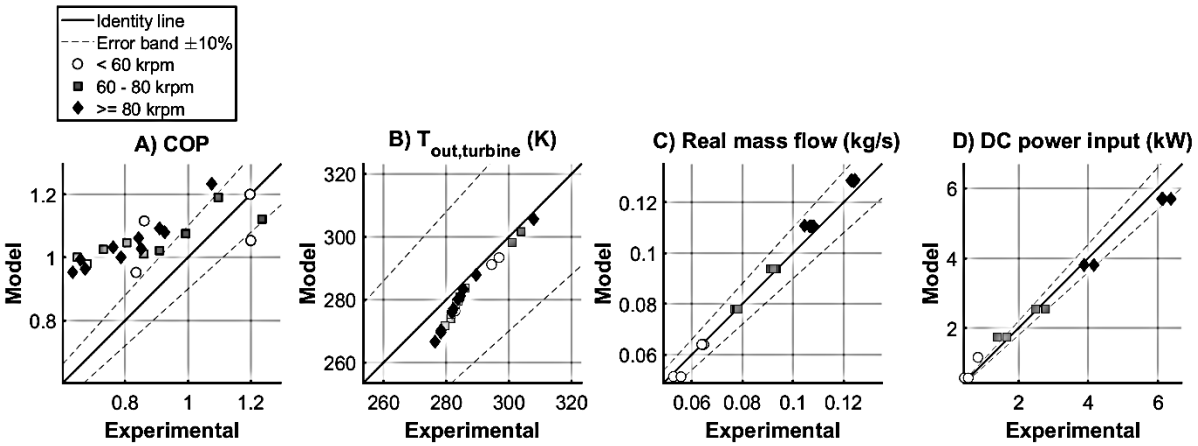

Figure. 10. *Model and experimental data parity analysis regarding the main performance indicators and operational values: a) COP, b) $T_{out,t}$, c) Real mass flow, and d) DC power input.*

As is possible to verify by analysing Figure 10, in general, the model showed a good agreement with the experimental results. It is possible to verify that the majority of deviations occurred for the higher motor velocities, while most indicators were still within the 10% error band. This disparity was more noticeable for COP values. This is a result of the cumulative error regarding the observable overestimation of the real mass flow and the underestimation of the $T_{out,t}$ and $\dot{P}_{DC}$. Nevertheless, these results should be taken into account carefully since most of the considered points fell within the 0.8 to 1.2 range, which still represents relatively high COP values for this type of system. It is important to notice that for the real mass flow, the error does not show a pattern of over- or underestimation. Nevertheless, for the outlet temperature, the model showed a consistent overestimation. This can be connected with the fact that real ambient air has humidity that at lower temperatures condenses, which could produce this result, or to the fact that there are heat gains in the turbine from the heat dissipation fluid that is at a higher temperature. It is also relevant to notice that for specific points for the lower motor speeds, the model tends to slightly underestimate COP and real mass flow values and overestimate the $\dot{P}_{DC}$.

4. Conclusions

This study provided a preliminary assessment of an off-the-shelf fuel-cell turbocompressor for low and ultra-low temperature (ULT) refrigeration. For that purpose, a semi-empirical thermodynamic model was developed and validated against experimental data from a custom-built test rig. Sensitivity and parametric analyses identified motor speed and turbine inlet temperature as the most critical variables, both exhibiting an inverse relationship with the Coefficient of Performance (COP). The Air Refrigeration Cycle (ARC) exhibited high potential for the low and ULT refrigeration, where high GWP refrigerants are mostly used. The model results also show, for the lower temperature stages, that a relatively high compound COP value could be achieved when compared with a standalone VCRC.

Regarding the experimental results, they could confirm the model's fundamental assumptions, notably the negligible pressure loss between the compressor and turbine and the high isentropic efficiencies of both components. The data also quantified the trade-off between increased motor speed, which enhances cooling capacity, and the resulting decline in COP. A parity analysis demonstrated high predictive accuracy, with errors generally below 10% for most parameters. The higher discrepancies observed in COP estimation are credited to cumulative residuals in mass flow and outlet turbine temperature, which could be attributed to the exclusion of water condensation and heat transfer phenomena simplifications in the current model. This justifies the extrapolation to temperatures where CCC becomes viable reached in the modelling.

Future research will focus on refining the model by addressing the considered simplifications, alongside with extending experimental validation to lower temperature ranges to fully demonstrate the system's potential.

Acknowledgments

This research was supported by the European Regional Development Fund of the European Union through the Innovation and Digital Transition Program (COMPETE 2030) of Portugal 2030 under the project Bio-Waste2Carbon (BW2C): Cryogenic carbon capture of post-combustion gases from forestry residues, contract number COMPETE2030-FEDER-00591900 (https://sustainc.com/pt/id/bio-waste2carbon); and by the Fundação para a Ciência e a Tecnologia, I.P. (https://ror.org/00snfqn58) under the UID/50022/2025 (https://doi.org/10.54499/UID/50022/2025) project.

Nomenclature

h enthalpy, kJ/kg

P pressure, kPa

T temperature, K

$\dot{m}$ real mass flow rate, kg/s

$\dot{m}_{corrected}$ corrected mass flow, kg/s

$\dot{m}_{reduced}$ reduced mass flow, kg ($K^{0.5}$)/(s kPa)

$\dot{P}_{DC}$ DC power input, kW

COP coefficient of performance

$\dot{W}$ work, kW

PR pressure ratio

Greek symbols

η efficiency

ω motor speed, krpm

Subscripts and superscripts

out outlet

in inlet

$isen$ isentropic assumption

$real$ real condition

t turbine

c compressor

References

[1] Ozden A, Luo M, Lum Y. Point-source carbon capture and direct air capture – A technology overview. Chemical Engineering Journal 2025;519. https://doi.org/10.1016/j.cej.2025.165535.

[2] Wanison R, Hadi Syahputra WN, Kammuang-lue N, Sakulchangsatjatai P, Terdtoon P, Tippayawong N, et al. A review of cryogenic carbon capture research: Experimental studies, simulations, and application potential. Thermal Science and Engineering Progress 2025;61. https://doi.org/10.1016/j.tsep.2025.103562.

[3] Font-Palma C, Cann D, Udemu C. Review of Cryogenic Carbon Capture Innovations and Their Potential Applications. C (Basel) 2021;7:58. https://doi.org/10.3390/c7030058.

[4] Low GWP Refrigerants – A Guide to Sustainable Cooling 2026. https://www.aaon.com/resources/low-gwp-refrigerant (accessed March 25, 2026).

[5] The Kigali Amendment (2016): The amendment to the Montreal Protocol agreed by the Twenty-Eighth Meeting of the Parties (Kigali, 10-15 October 2016) | Ozone Secretariat 2026. https://ozone.unep.org/treaties/montreal-protocol/amendments/kigali-amendment-2016-amendment-montreal-protocol-agreed (accessed March 25, 2026).

[6] Saeed MZ, Contiero L, Blust S, Allouche Y, Hafner A, Eikevik TM. Ultra-Low-Temperature Refrigeration Systems: A Review and Performance Comparison of Refrigerants and Configurations. Energies (Basel) 2023;16. https://doi.org/10.3390/en16217274.

[7] Mota-Babiloni A, Mastani Joybari M, Navarro-Esbrí J, Mateu-Royo C, Barragán-Cervera Á, Amat-Albuixech M, et al. Ultralow-temperature refrigeration systems: Configurations and refrigerants to reduce the environmental impact. International Journal of Refrigeration 2020;111:147–58. https://doi.org/10.1016/j.ijrefrig.2019.11.016.

[8] Refrigeration - Climate-friendly alternatives to F-gases – Climate Action 2026. https://climate.ec.europa.eu/eu-action/fluorinated-greenhouse-gases/climate-friendly-alternatives-f-gases/refrigeration_en (accessed March 25, 2026).

[9] Biglia A, Bilardo M, Comba L, Ricauda Aimonino D, Grella M, Fabrizio E, et al. Performance analysis of a nitrogen-based Brayton cryocooler prototype. Energy 2024;290. https://doi.org/10.1016/j.energy.2023.130095.

[10] Dhillon AK, Ghosh P. Exergoeconomic evaluation and optimization of reverse Brayton refrigerator. Journal of Energy Resources Technology, Transactions of the ASME 2021;143. https://doi.org/10.1115/1.4050877.

[11] Rong W, Ma G, Sun S, Xu S, Tian Y, Yu G. Simulation study on two-stage compressed air cycle refrigeration system with blower. Renew Energy 2026;256. https://doi.org/10.1016/j.renene.2025.124318.

[12] Whelan CD, Richards RA, Spence SWT, Young A. Design and development of a turbo-expander for charge air cooling. 9th International Conference on Turbochargers and Turbocharging - Institution of Mechanical Engineers, Combustion Engines and Fuels Group, Woodhead Publishing Ltd.; 2010, p. 459–70. https://doi.org/10.1243/17547164C0012010035.

[13] Antivachis M, Dietz F, Zwyssig C, Bortis D, Kolar JW. Novel High-Speed Turbo Compressor With Integrated Inverter for Fuel Cell Air Supply. Front Mech Eng 2021;6. https://doi.org/10.3389/fmech.2020.612301.

[14] Products | FISCHER Fuel Cell Compressor AG 2026. https://www.fischer-fuelcell-compressor.com/en/products (accessed March 25, 2026).

[15] Lemmon EW, Bell IH, Huber ML, McLinden MO. NIST Standard Reference Database 23: Reference Fluid Thermodynamic and Transport Properties-REFPROP, Version 10.0, National Institute of Standards and Technology 2018. https://doi.org/https://doi.org/10.18434/T4/1502528.